



Rapid, deep dopant diffusion in crystalline silicon by laser-induced surface melting[☆]

Zibo Zhou^{a,*}, Ivan Perez-Wurfl^a, Brian J. Simonds^b

^a School of Photovoltaic and Renewable Energy Engineering, Faculty of Engineering, UNSW Australia, Kensington, NSW 2052, Australia

^b Applied Physics Division, National Institute of Standards and Technology, Boulder, CO 80305-3337, United States

ABSTRACT

As solar cell back contact schemes have improved in recent years, the non-ideal emitter region has become a dominant contributor to overall losses in solar cell efficiency. Our analysis shows that these losses can be greatly reduced by creating a lightly ($< 10^{18} \text{ cm}^{-3}$), uniformly doped emitter that is about $10 \mu\text{m}$ deep. However, the constraints imposed by current manufacturing techniques, namely using a tube-furnace for solid state dopant diffusion, limits the emitter to a much more highly doped ($\sim 10^{20} \text{ cm}^{-3}$) and shallow ($< 500 \text{ nm}$) region. A laser-based process by which dopants are diffused in a liquid silicon state can overcome these limitations. In this work, we provide semiconductor device simulations that compare the effects of these two types of emitters on device performance. Then, we used a heat transport model to demonstrate that a focused laser line beam can create a molten region at the surface of a silicon wafer that would allow dopants to diffuse deeply within a short amount of time. We then performed the laser processing with a scanned laser line beam on preheated silicon samples. The resulting junction depth ($> 10 \mu\text{m}$) is measured by cross-sectional etching and electron beam-induced current measurements. Electrochemical capacitance-voltage measurements are used to measure both the depth as well as the dopant profile resulting from the laser-driven process. We also analyse dislocation defects induced by the large thermal gradients inherent to the laser-based process which would greatly limit the device performance.

1. Introduction

A typical commercial, front-junction solar cell contains a p-type substrate with a thermally-diffused, phosphorus-doped (n-type) emitter [1,2]. Electrically, the emitter's primary effects on solar cell performance are in determining the open-circuit voltage (V_{oc}) and the collection probabilities of photogenerated carriers [3]. A typical emitter is a few hundred nanometers thick and contains a high peak level of dopants (10^{20} cm^{-3}). This design is a compromise between device performance, which calls for a deeper, low-doped emitter, and the time and cost it would take to manufacture such a region. High doping levels are necessary in thin emitters to achieve acceptable lateral conductivity, screen carriers from the relatively high surface recombination velocity, as well as to facilitate the formation of Ohmic contacts [1]. This comes at the cost of very-short diffusion lengths (a few hundred nm) due to high Auger recombination. In practice, this unoptimised emitter design is tolerated as recombination at the rear of current commercial solar cell architectures dominates losses and consequently dominates the dark saturation current, J_0 [4]. As a result, the added

production costs involved in improving the emitter would result in only a negligible overall improvement to J_0 . However, new back contact schemes like oxide point contacts [5–7] or the ultra-thin tunnelling oxide contacts in so-called TOPcon cells [8,9], dramatically reduce the J_0 arising from recombination in the substrate. With these new designs, the standard heavily-doped, shallow emitter becomes a major factor limiting the conversion efficiency of the cell [10]. These emerging technologies require a better emitter design that does not compromise the cost of production or throughput [10,11].

A low recombination emitter that does not compromise lateral conductivity can be achieved with a lightly-doped (low-Auger recombination) and deep (low sheet resistance) emitter. The analysis in the following section shows that a roughly 10^{18} cm^{-3} emitter on the order of $10 \mu\text{m}$ thick is optimal for device performance. It is possible to achieve such depths with traditional POCL furnace annealing, but solid-state diffusion will require tens of hours to reach this thickness. This is an untenable approach for commercial solar cell manufacturing that cannot afford such a time-intensive process. Pulsed laser processing has been used to quickly drive dopants into Si by melting a surface region,

[☆] This work of the U.S. Government is not subject to U.S. copyright.

* Corresponding author.

E-mail address: zib.zhou@gmail.com (Z. Zhou).

but these depths have thus far been limited to less than 1 μm due to the short pulses being used (~ 100 ns) [12–14]. In order for a laser process to achieve depths on order of 10 μm , the dwell time needs to be significantly increased as the heat affected region scales with the square root of laser exposure time [15]. Therefore, in this paper we investigate a scanning continuous-wave (CW) laser process to create such a junction by melting the surface of initially shallow-doped silicon wafers, thereby causing the dopants to be redistributed within the melt pool in a very short amount of time (here, about 40 ms laser dwell time). Furthermore, industrial CW diode line lasers are currently manufactured with beam widths as high as 30 cm, making this approach viable for industrial high-throughput, inline manufacturing.

The aim of this work is to provide the foundational research towards realizing a low-doped, deep emitter solar cell by demonstrating a CW laser process that is in principle compatible with commercial solar cell production. Fully realizing a competitive solar cell based on this new processing approach with the subject of further research and development. The first part of this paper provides a theoretical justification for the pursuit of a deep, low-doped emitter, and that a CW laser is capable of providing such a junction. Then, we experimentally demonstrate that a deep, low-doped emitter can be formed by a CW laser melting process. Next, we investigate the resulting laser-induced defects. As these defects will ultimately limit the eventual device performance, we discuss possible solutions to mediate these at the end of the final section.

2. Theory

2.1. Modelling device performance of a deep junction

In order to illustrate the benefits of having a deep and lightly-doped emitter on a rear-passivated Si solar cell, a series of two-dimensional (2D) simulations were performed using COMSOL Multiphysics software [16,17]. 2D simulations are minimally necessary to capture the effects of lateral current flow. The geometry of the simulated structures is presented in Fig. 1, and is modelled after a passivated emitter and rear cell (PERC) geometry [18]. The wafer is 175 μm thick, the front contact finger pitch and width are 1 mm and 60 μm [19], respectively (6% shading loss). The unit cell was chosen to be half of the finger pitch, which is 500 μm . Localised aluminium back surface fields (BSF) are modelled by two heavily-doped, Gaussian distributed, p-type regions that are 2.5 μm wide, which amount to 1% of the total rear surface area. Due to the restrictions imposed by a 2D simulation, we assume a strip rear-contact instead of the point contact structure of real PERC cells, which likely underestimates the effects of bulk spreading resistance [20]. The out-of-plane thickness is defined as 1 cm such that the surface area of the simulated device is 0.05 cm^2 . We only consider the electrical resistance arising from drift current in the silicon wafer and exclude the resistance in metal and the contact resistance (solved for pseudo fill factor, pFF) at this stage. After the emitter being optimised, the contact

resistance can be minimised by applying the selective emitter technology on the lightly doped surface [21,22].

Maxwell-Boltzmann carrier statistics were considered using a finite volume (constant shape function) method as the numerical solver. The number of degrees of freedom for the finite volume method is twice that of the finite element method with a 2D linear shape function, thus providing higher accuracy [23]. The partial differential equations solved in the semiconductor model are listed below:

$$\nabla \cdot (-\epsilon_r \nabla V) = q(p - n + N_d^+ - N_a^-), \quad (1)$$

$$\nabla \cdot J_n = -qU_n, \quad \nabla \cdot J_p = -qU_p, \quad (2)$$

$$J_n = qn\mu_n \nabla E_c + \mu_n k_B T \nabla n + qnD_n^{\text{th}} \nabla \ln(T), \quad (3)$$

$$J_p = qp\mu_p \nabla E_c + \mu_p k_B T \nabla p + qpD_p^{\text{th}} \nabla \ln(T), \quad (4)$$

$$E_c = -(V + X_0) - \alpha \Delta E_g, \quad (5)$$

$$E_v = -(V + X_0 + E_{g,0}) + (1 - \alpha) \Delta E_g. \quad (6)$$

Eq. (1) is Poisson's Eq. (2) is the current continuity Eqs.; (3) and (4) are the drift-diffusion equations for electrons and holes, respectively; (5) and (6) describe the band structure with respect to the vacuum level, $-V$. These equations are solved for the electron (n) and hole (p) concentrations, as well as the potential, V , where T is temperature, q is elementary electric charge, k_B is Boltzmann constant, $U_{n,p}$ is the lumped recombination rate (including Auger, SRH, optical generation etc.), $J_{n,p}$ is the current density, $D_{n,p}^{\text{th}}$ and $\mu_{n,p}$ are the diffusion coefficient and carrier mobility for electrons and holes respectively. Some of the parameters are defined in Table 1. Bandgap narrowing is considered as described by the Slotboom equation [24]:

$$\Delta E_g = E_{\text{ref}} \left(\ln \left(\frac{N_d + N_a}{N_{\text{ref}}} \right) + \sqrt{\left(\ln \left(\frac{N_d + N_a}{N_{\text{ref}}} \right) \right)^2 + \frac{1}{2}} \right) \quad (7)$$

where N_d and N_a are doping densities and N_{ref} and E_{ref} are concentration and energy references, respectively. As can be seen, the Slotboom model is independent of carrier injection level. The calculated ΔE_g is then used to determine the conduction and the valence band edges, E_c and E_v .

As seen in Eq. (5), by subtracting the electron affinity and ΔE_g from the vacuum level, we obtain the energy of the bottom of the conduction band. In our model, bandgap narrowing affects the conduction and valence band equally ($\alpha = 0.5$).

Shockley-Read-Hall (SRH) and Auger recombination are considered for the entire structure. The SRH recombination rate is determined according to references [25,26] and is parameterized by an electron lifetime, τ_n . Auger recombination rates are calculated according to the formulation described in [27], and is parameterized according to electron and hole recombination factors, C_n and C_p . These, as well as

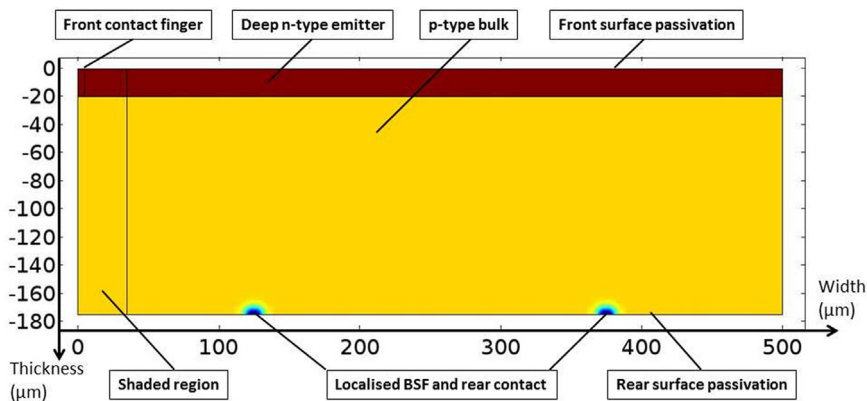


Fig. 1. Solar cell geometry used for semiconductor physics simulations.

Table 1
Electronic material properties for semiconductor simulations.

Property	Value	Unit
Relative permittivity, ϵ_r	11.9	1
Auger recombination factor, electrons (C_n)	2.20×10^{-31}	m^6/s
Auger recombination factor, hole (C_p)	9.90×10^{-32}	m^6/s
Electron lifetime, SRH (τ_n)	500	μs
Band gap (E_{g0})	1.124	V
Electron affinity (χ_0)	4.05	V
Band-gap narrowing reference energy (E_{ref})	0.009	V
Band-gap narrowing reference concentration (N_{ref})	1.00×10^{17}	$1/\text{m}^3$
Conduction band fraction (α)	0.5	1

other parameters used in the semiconductor simulations, are found in Table 1.

For the front contacts, one-sixth of the contact area is assumed to be ideally Ohmic with a corresponding infinite surface recombination velocity (SRV), while the rest is passivated with an insulating (oxide) layer. This approximates the actual scenario where the screen-printed contacts are partially passivated by glass with a thermal velocity-limited SRV well below 10^7 cm/s [28,29]. In order to simulate a device passivated by thermal oxide, the non-contacted front SRV is considered a function of surface dopant concentration as parameterized in [30]. The non-contacted rear surfaces are given a SRV of 10 cm/s, which is consistent with results from state-of-the-art passivation techniques with silicon nitride or aluminium oxide stacks [31–33]. The substrate wafer was assigned a background doping of 1×10^{16} cm $^{-3}$ and a Shockley-Read-Hall lifetime of 500 μs [34,35]. The peak dopant concentration of the localised BSF region is 1×10^{18} cm $^{-3}$ with a depth of 12 μm [36]. A carrier density-dependent mobility was used as described in [37]. The carrier generation profile in the unshaded region is determined by the online tool OPAL2 available at PV Lighthouse [16,38]. The temperature is set to 300 K. During the solving process, the voltage at the rear contact is swept to obtain a current-voltage curve for the device. All other parameters are held fixed to determine the effects of emitter thickness, doping level, and profile on the performance of the cell.

Simulation results are shown in Figs. 2–4 for the above device geometry. Fig. 2 shows simulation results for a cell that has a 500 nm thick, Gaussian profile emitter which is representative of an industrial PERC cell and will be referred to as the “reference cell.” Plotted are the predicted efficiency and open-circuit voltage (V_{OC}) values versus the peak doping level. A black vertical line at 4×10^{19} cm $^{-3}$ peak doping level indicates the lower-end of the doping range that is typically achievable by the industrial tube furnace method [39]. This higher-than-optimum dopant concentration is required in practice in order to achieve a laterally homogenous doping profile by the tube furnace method. The simulated V_{OC} for the reference cell, around 660 mV, is consistent with that of other simulated or industrially produced high-end PERC cells with a laterally homogenous emitter [18,19,31,34,35,40,41]. The results shown in Fig. 2 show that the limitations imposed by tube furnace manufacturing for PERC cells result in an absolute efficiency loss of about 1%.

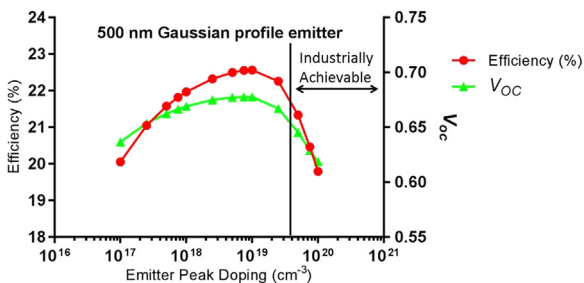


Fig. 2. COMSOL simulation results for PERC cells with tube furnace diffused emitter as a reference, at different peak doping density.

In the next simulations, we compare the effects of emitter dopant concentration and emitter layer thickness on cell efficiency and V_{OC} for a uniformly doped emitter. We assume a uniformly doped emitter due to the high diffusion coefficient of P in liquid silicon [42,43]. These results are shown in the contour plots of Fig. 3 and Fig. 4, which give a predicted optimum value of dopant concentration and emitter thickness as 5×10^{17} cm $^{-3}$ and 8 μm , respectively. When the dopant concentration is lower, sheet resistance increases and the V_{OC} drops due to increased emitter recombination and the efficiency drop due to increased resistive losses due to lateral current flow. However, over-doping leads to severe bandgap narrowing, increased Auger recombination, and less effective front surface passivation. Therefore, doping level and emitter thickness optimization is a trade-off between majority carrier transport and recombination rate. The lightly-doped, deep emitter balances these two effects, providing superior performance over a traditional furnace diffused emitter. In comparison to the reference cell data given in Fig. 2, such an emitter would provide an absolute efficiency increase of 0.6% over the PERC cell with an ideal Gaussian emitter and a 1.5% increase over one with an emitter typically produced by a tube furnace.

2.2. Heat transfer simulation of laser melting process

In order to reach the optimum emitter thicknesses demonstrated in the previous section in a reasonable amount of time, diffusion of the dopants needs to occur in Si while in a liquid state. This stems from the fact that the diffusivity of P in liquid Si is over 9 orders of magnitude larger than in solid Si at 1000 °C (5×10^{-4} cm $^2/\text{s}$ versus 1×10^{-13} cm $^2/\text{s}$ assuming a dopant concentration of 10^{20} cm $^{-3}$) [42,43]. Therefore, the approach here is to melt a thin, dopant containing surface layer, whereby upon melting the dopants are rapidly, and uniformly, redistributed in the melt. Creating this molten layer calls for the application of a local, high-energy density, and rapid heat source as can be given by a laser beam. In this section, we use a 2-dimensional thermophysical model to demonstrate that a laser beam is capable of reaching the target melt depths discussed previously.

We created a 2-dimensional model that consists of a 500 μm thick Si wafer in contact with a 5 mm piece of iron whose back surface is held fixed at 650 °C. This arrangement closely replicates the situation used in our experiments where a hotplate is used to preheat the Si wafer. The interface between these surfaces is parameterized by a thermal contact conductance that was optimised through comparison with optical temperature measurements. These were performed with a two-colour infrared pyrometer sensitive to 1.52 and 1.64 μm wavelengths, which focused at the centre of a Si wafer during a laser scan. The temperature range of this device was limited to below 1300 °C, which meant that only solid Si could be measured for contact conductance optimization.

Heat was assumed to be completely absorbed at the surface simulating a laser wavelength well-above bandgap. The heat source was moved along the surface of the Si layer in the x-direction with a speed of 6.67 mm/s. Our experimental laser beam profile is a line that has a top hat in the long direction and is Gaussian in x. Therefore, the spatial profile in the x-direction of the applied heat source was

$$I(x) = \left(\frac{P}{\sqrt{2\pi} \sigma_x L} \right) \left(e^{-x^2/2\sigma_x^2} \right) W/m^2 \quad (8)$$

where P is the total laser power, σ_x is the standard deviation of the Gaussian beam in the x-direction, and L is the length in the y-direction. The temperature through the thickness was calculated by solving the heat-transfer equation as detailed in reference [44].

A comparison of the measured temperatures and temperature gradients to those predicted for a 115 W laser scan are given in Fig. 5a. The small discrepancy in peak temperature is expected as the area over which the temperature is measured is determined by the spot size of the focusing optics of the pyrometer, which is 1.2 mm in our case.

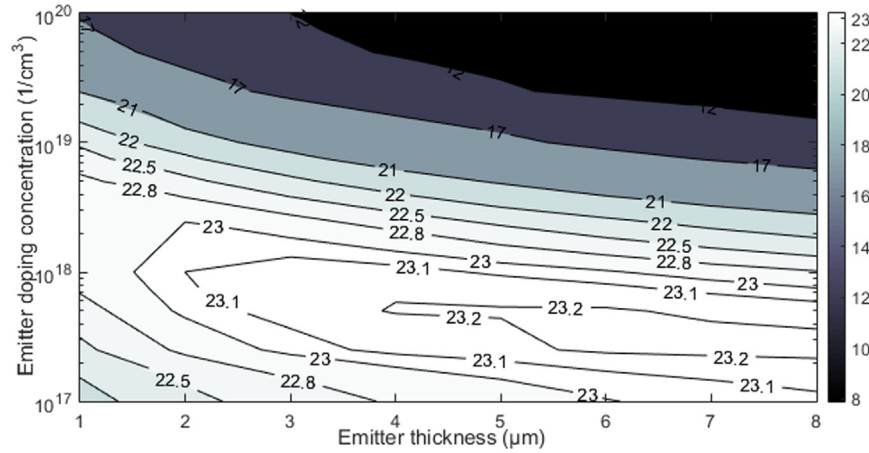


Fig. 3. Simulated PERC cell's efficiency (%) with low recombination emitters as a function of the emitter thickness and doping concentration (uniform doping profile).

Additional thermophysical properties used in the simulation are given in Table 2. Fig. 5b. shows the predicted melt depth as a function of input power with the onset of melting occurring between 150 and 160 W. These results clearly show that the desired melt depths necessary for deep dopant diffusion can be readily achieved by a scanned laser line beam.

3. Experimental set-up

The laser melting was achieved by using a high-power 808 nm diode laser as shown in Fig. 6. Line beam shaping was accomplished using commercial beam-shaping optics that achieved a top-hat profile in the long dimension of 12.1 mm full width at half maximum (FWHM) with a steep intensity gradient at the edge of 3 mm. The beam was Gaussian in the short dimension of 270 μm (full width at $1/e^2$). The laser line was scanned over the silicon substrate at a rate of 6.67 mm/s. This corresponds to a laser dwell time of about 40 ms. As proof-of-principle, this paper focuses mainly on experimental results from samples treated in the 220–250 W range, which corresponds to the range in Fig. 5b predicted to give melt depths for maximum solar cell performance in Fig. 3 and Fig. 4. Future works will provide a more exhaustive study of the effects of varying process parameters. The substrate was placed on a hotplate at 650 °C to reduce the large temperature gradients, and accompanying thermal stresses, that are induced during laser processing.

For our experiments, we used p-type, 1–10 Ωcm , 500 μm thick,

(100)-oriented, 100 mm (4 in.) diameter double-sided polished Czochralski Si wafers. In order to control the amount of dopants introduced to the wafers, phosphorus dopants (around $4.3 \times 10^{14}\text{ cm}^{-2}$) were introduced in a POCl_3 tube furnace followed by a phosphosilicate glass removal step. In principle, this time-consuming step could be replaced by spin-coating a layer of phosphoric acid once the process has been optimised. All wafers went through a standard RCA clean before high temperature processing. The wafers were then laser cut into pieces either 1 cm or 2 cm wide, and up to 3 cm long. The stated laser power in this work is based on the manufacturer relating the pump laser diode current to the fiber laser output power. The calibration was done using a water-cooled broadband thermopile detector that can measure from 50 W to 1000 W with a manufacturer-specified 5% uncertainty over this range.

Several measures of junction depth were performed. The first was the Yang defect etching technique, which differentially etches p- versus n-type Si [68]. This technique was used on cross-sectioned samples following laser treatment and was particularly useful given its relatively high etch rate, controllability and simplicity [69,70]. The method works via a two-step process [71]. First, CrO_3 in a solution with hydrofluoric acid (HF) oxidizes the silicon with a rate dependent on the doping type and also type of defect site it interacts with. Second, high concentration HF removes the silicon oxide resulting in a visual contrast between defect sites and the surrounding crystal. This step is performed for 2 min with manual agitation. After the process was

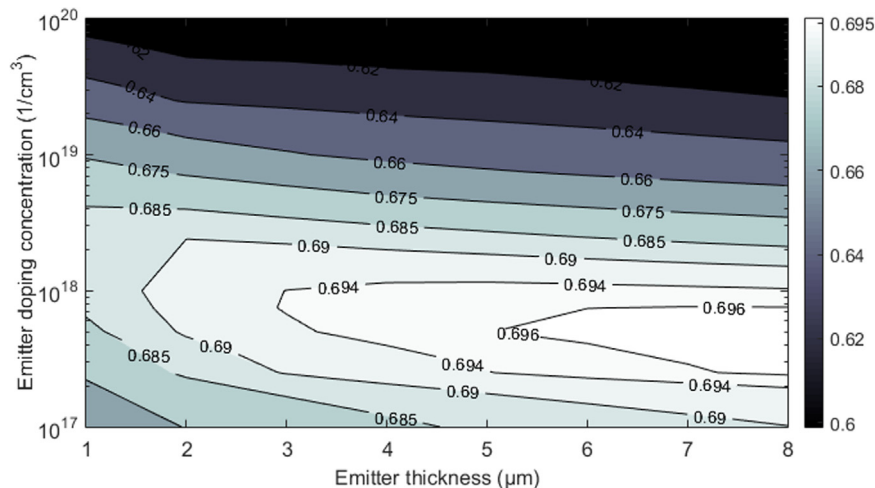


Fig. 4. Simulated PERC cell's V_{OC} (V) with low recombination emitters as a function of the emitter thickness and doping concentration (uniform doping profile).

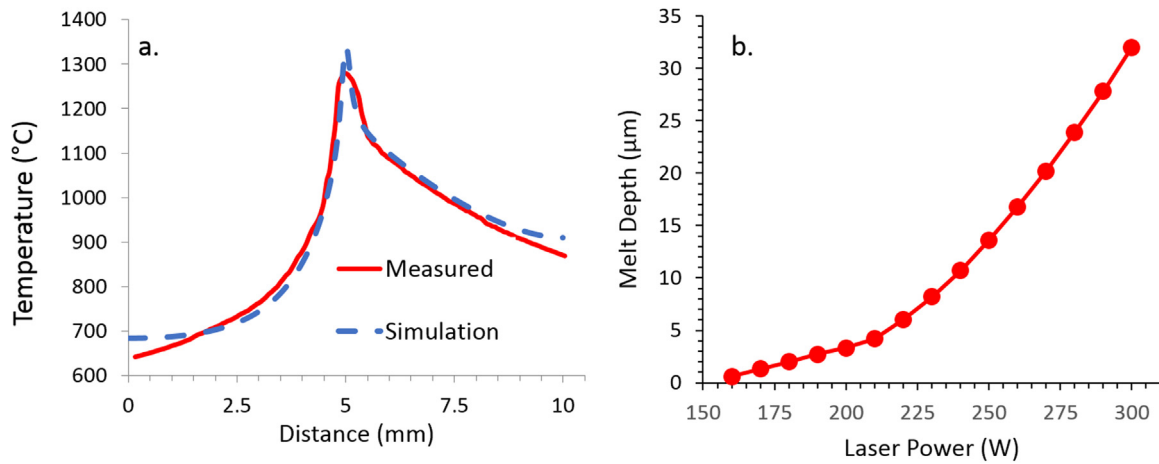


Fig. 5. Predicted temperatures for 115 W laser heating compared to experimental results (a.) and melt depths versus applied laser power (b.).

Table 2

Properties and parameters used in the thermal simulations.

Property	Value	Comments/references
Emissivity, Absorptivity, and (1 – Reflectivity)	0.68 0.28	Solid [45,46] Liquid [47]
Heat Capacity, Si (J/g K)	$(0.158 + 3.13 \times 10^{-3} \cdot T - 5.60 \times 10^{-6} \cdot T^2 + 5.22 \times 10^{-9} \cdot T^3 - 2.40 \times 10^{-12} \cdot T^4 + 4.29 \times 10^{-16} \cdot T^5)$ J/(g K)	Solid [48]
Density, Si (kg/m ³)	0.9685 J/(g K) $(2330 + 0.484 \cdot T + 1.98 \cdot T^2)$ kg/m ³ $(2885 - 0.1925 \cdot T)$ kg/m ³	Liquid [48] Solid [49]
Thermal Conductivity, Si [W/m K]	$(95.44 - 0.0969 \cdot T + 3.27 \times 10^{-5} \cdot T^2)$ W/(m K)	Liquid ^a [49–58] Solid ^a [59–61]
Contact conductance	50 W/(m K)	Liquid [59]
Melting Point, Si	2000 W/m ² K	Empirically optimised
Latent Heat, Si	1683 K	[62–64]
Density, Fe	1779 kJ/kg	[48,64]
Thermal Conductivity, Fe	7870 kg/m ³	[65]
Heat Capacity, Fe	76.2 W/(m K)	[66]
	440 J/(kg K)	[67]

^a Denotes that this is an average of multiple literature values if a single value is given, or it is from a linear fit of multiple literature values if a functional form is given.

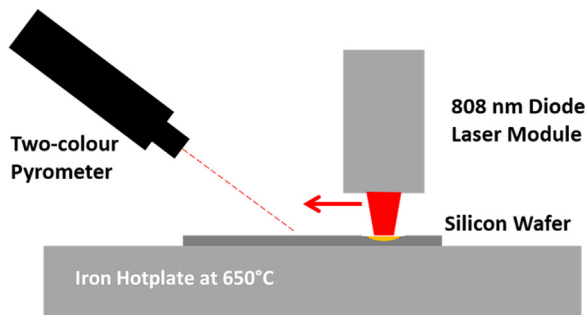


Fig. 6. Diagram of laser annealing experiment.

completed, the difference in etch rate created a contrast in the cross-section at the point of the electrical junction that was imaged and measured using a scanning electron microscope. Additionally, Yang etching was also used to identify dislocation defects [68] throughout the melt and substrate regions. These measurements were performed on samples treated with 222 W and 246 W.

Electron beam-induced current (EBIC) measurements [72] were also performed in order to provide evidence of laser-induced deep junction formation on a sample treated with 234 W. Thin aluminium layers were thermally evaporated on both sides of the sample to extract the electron induced current. An electron beam was swept on the cross-section of the sample near the laser processed front surface and a contrast formed at the pn-junction as the carrier collection probability there is higher.

The dopant profile of the 246 W treated sample was measured with electrochemical capacitance-voltage (ECV) measurements [73]. These measurements also confirmed the junction depth measured with cross-sectional etching. An HF dip was performed prior to the measurement to minimise the interference from native oxide. The measurement was taken at the centre of the laser processed region where a homogenous emitter is formed. The sheet resistance was measured using a standard 4-point probe technique [74] over a wide range of laser powers.

4. Experimental results and analysis

4.1. Deep junction formation

Evidence of deep-dopant diffusion is given by the cross-section images shown in Fig. 7. This image follows the application of a Yang etch process of a sample treated with 246 W of laser power. A sharp contrast appears in the image at 13.7 μm from the sample surface that marks the location of the pn-junction. This junction depth agrees well with the melt depth of 13.6 μm for 250 W predicted in our model in Fig. 5b.

Confirmation that the demarcation line in Fig. 7 is created by the pn-junction interface is provided by ECV measurements on a similarly prepared sample. These are shown in Fig. 8 where the P dopant concentration versus depth is plotted on a log-log plot for a sample laser-treated at 246 W along with that of the sample before laser melting. The concentration appears largely uniform over most of its depth at about $5 \times 10^{17} \text{ cm}^{-3}$ with a depth of 14.3 μm for the laser-processed sample.

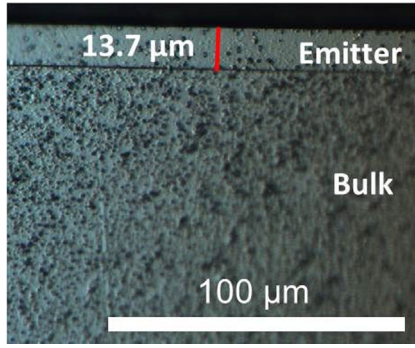


Fig. 7. The cross-sectional image (CSs) of a sample treated with 246 W after Yang etching (500×). The top layer which contains fewer dislocation pits is the recrystallized emitter, which is 13.7 μm thick.

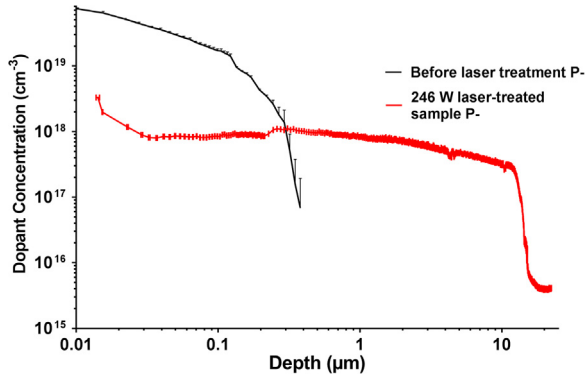


Fig. 8. Phosphorus concentration as a function of depth (where the vertical lines are error bars) determined by ECV for a 246 W laser-treated sample compared to an unprocessed sample that has a traditional emitter formed by solid state furnace diffusion.

The depth agrees well with that predicted by the etch cross-sections as well as the melt depth given by the thermal model. Also, the dopant concentration is near the optimal value determined in our model given in Fig. 3 and Fig. 4.

Further evidence of laser-driven deep dopant diffusion is provided by EBIC measurements given in Fig. 9. These were performed on a sample treated with 234 W. The junction is identified by the horizontal line that appears bright as the carrier collection probability is highest in the junction region. The junction depth shown here is 12.7 μm below

the surface. Considering that a slightly lower laser power was used here than that used in Fig. 7 and Fig. 8, we find that the junction depth is in good general agreement. The EBIC image also shows a very laterally uniform junction, which is consistent with the cross-sectional image shown in Fig. 7.

The deep, low-doped emitter shown to result from the laser process in Fig. 8 and Fig. 9 should also increase the electron mobility, μ_n , in the emitter (reduced carrier-carrier scattering) via the relationship [1]:

$$\mu_n = 65 + \frac{1265}{1 + \left(\frac{n}{6.3 \times 10^{16}}\right)^{0.72}} \text{ cm}^2/\text{Vs} \quad (9)$$

In turn, this reduces the sheet resistance from the relationship shown in Eq. (10), where n is the doping concentration, t is the emitter thickness and Q is the total amount of the dopant in the emitter [1]:

$$R_s = \frac{1}{q \cdot \mu_n \cdot n \cdot t} = \frac{1}{q \cdot \mu_n \cdot Q} \quad (10)$$

Therefore, a measure of sheet resistance, R_s , as a function of laser processing power can provide a qualitative indication of a laser-formed deep, low-doped emitter. Four-point probe measurement of R_s are shown in Fig. 10. The sheet resistance before laser treatment is around 100 Ω/sq. This remains approximately unchanged for laser treatments below about 200 W, at which point the sheet resistance drops roughly linearly with laser power. The drop in R_s near 200 W can be explained by the onset of deep laser melting (> 3 μm) and recrystallization and the resultant deep, low-doped emitter as will be discussed further in a later section.

4.2. Material effects from laser melting

Given the extreme temperature gradients achieved during this laser process, it is expected that thermal stress-induced defect formation can accompany the deep dopant diffusion demonstrated in the previous section. Visual observations of the sample surfaces following laser treatment in three different power regimes is given in Fig. 11. Fig. 11a is representative of a low-power treated wafer surface for laser powers below 150 W. A pockmarked surface is indicative of a silicon wafer treated at laser powers between 150 and 220 W (Fig. 11b). Finally, at laser powers above 220 W a smooth, planar surface returns which we believe is indicative of a fully recrystallized surface. Our finite element simulations presented in Fig. 5b show that melting begins at between 150 and 160 W, which coincides with the surface changes seen in Fig. 11b. The appearance of a greatly smoothed surface in Fig. 11c at powers greater than 220 W is near the point in Fig. 5b where the melt



Fig. 9. SEM + EBIC image for bare silicon sample 226 treated with 234 W. The junction depth was measured to be 12.7 μm as shown by the red arrow. (For interpretation of the references to color in this figure legend, the reader is referred to the web version of this article.)

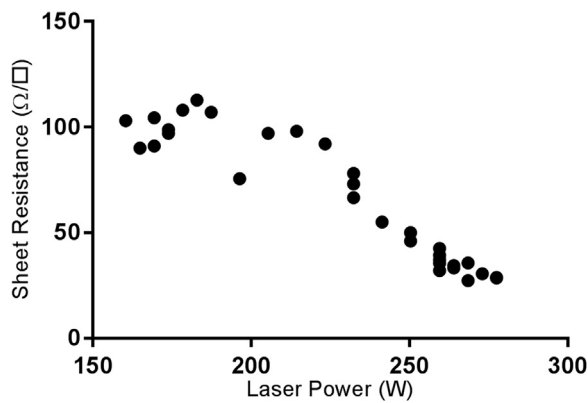


Fig. 10. Measured sheet resistance as a function of applied laser power.

depth is about 3 μm and increases much more rapidly with power than at lower powers. Therefore, it appears that a smooth, planar surface could be indicative of very deep ($> 3 \mu\text{m}$) melting. Furthermore, this observation is consistent with the hypothesis that the onset of the steep decrease in R_s is a result of greatly reduced dopant concentrations as a result of deep melting.

The Yang defect etching technique used previously to discern the junction depth in cross-section can also be used to investigate and identify dislocations at the laser treated silicon surface. Although Si is a brittle material at room temperature, above the brittle-to-ductile transition temperature (around 600–700 $^{\circ}\text{C}$) dislocations can occur at surfaces [75]. Fig. 12 shows the etching result of a representative surface treated with less than 150 W. One sees several teardrop-shaped etch pits which mark the sites of individual dislocations. Many of these pits connect forming dark vertical channels on the etched surface known as dislocation line [70]. This is a sign of the well-known phenomenon whereby a single dislocation can generate others as it moves through the Si lattice [76]. The pointed ends of the pits often terminate on slip planes (steps) [77], which are seen here as bright, narrow vertical lines. The observation that the density of the etch pits and the associated slip lines decreases at the edge of the laser scan area (Fig. 12b.) indicates that these dislocations are a result of thermal gradient-induced stress associated with laser processing. It is also worth noting that similar slip steps and dislocation pits are found on the back of the wafer directly underneath the laser processed area. This suggests that the slips propagate across the full thickness of the wafer.

Slip steps are the result of entire $\langle 111 \rangle$ crystal planes slipping to release the shear stress that occurs with high temperature gradients [78]. Prior to etching, one can see evidence of this slipping as vertical lines in Fig. 11a. The slipping of a $\langle 111 \rangle$ plane is achieved through the slipping of multiple dislocations on that particular plane. This effect has been witnessed previously resulting from the growth of Czochralski (CZ) ingots, which can suffer from large temperature gradients across the core and surface while cooling [79]. Fig. 13 shows a diagram of the active slip systems in silicon with respect to orientation of our

experiments. The slip steps seen at the wafer surface are always orientated in the $\langle 110 \rangle$ direction, which is the laser scan direction and parallel to the wafer primary flat. Dislocations in silicon tend to slip on (111) planes and in three directions for each plane (blue, doubled-sided arrows in Fig. 13) [76]. We observe lines along the $\langle 110 \rangle$ direction which would be slip steps at the intersection between the (100) wafer surface and two of the four (111) slip planes. In order to observe the (110) planes directly, etched cross-sections were prepared from two (110) planes: one parallel to the primary flat (CSp) and one parallel to the secondary flat (CSs). These cross-section images are found in Fig. 14. The slip lines on the CSp cross-section are all parallel to each other and parallel to the wafer surface, whereas the slip lines on the CSs cross-section intersect each other at a 70.4° angle as shown in Fig. 14. The predicted angle between lines that lie a (111) plane is $180^{\circ} - (54.74^{\circ} \times 2) = 70.52^{\circ}$, which is in good agreement with our measured value.

If dislocations slipped at all four (111) planes, the slip lines appearing on both CSp and CSs would be a mix of parallel and intersecting lines. In contrast, only one type is found for each cross-section demonstrating that only two (111) slip systems are active. This is consistent with the slip steps observed at the wafer surface. If the slip only occurred on (11 $\bar{1}$) and ($\bar{1}\bar{1}$ 1) planes (blue, double-sided, solid arrows), then the slip would only move along the three $\langle 110 \rangle$ directions shown in Fig. 13. A possible cause is that the shear strain induced by the laser is approximately normal to the other two (111) planes, ($\bar{1}\bar{1}$ $\bar{1}$) and (111) (red, double-sided, dotted arrows), so most of the stress is released through the movement of (11 $\bar{1}$) and ($\bar{1}\bar{1}$ 1) planes.

Another observation of the cross-sectional etching is that the bulk appears to have a higher dislocation density than the epitaxially regrown emitter region. At this point, we do not completely understand this phenomenon, but acknowledge that controlling it will be key to improving material quality and therefore device performance. As it is supposed that the large temperature gradients are the culprit, reasonable attempts at reducing them throughout the process should be pursued. One possible method that shows promise, is the use of a second, larger area laser beam to rapidly heat and control cooling of the sample before and after laser melting [44]. Our one-dimensional model estimated that a powerful areal laser (around 100 W/cm²) can further reduce the temperature gradient by two orders of magnitude if convection and radiation are the only heat loss mechanisms. Another approach is to increase the strain rate during laser processing by using a more powerful line laser with a much higher scan speed to limit the migration of dislocations [80,81]. Further investigation of these techniques will be the subject of future research.

5. Conclusion

We have demonstrated that a focused laser line beam can create a deep ($> 10 \mu\text{m}$), low doped ($< 10^{18} \text{ cm}^{-3}$), and uniform emitter. A finite-volume simulation comparing a solar cell device with such an emitter with a cell typical of that manufactured demonstrated that it could improve the overall device efficiency by 1.5% absolute. The

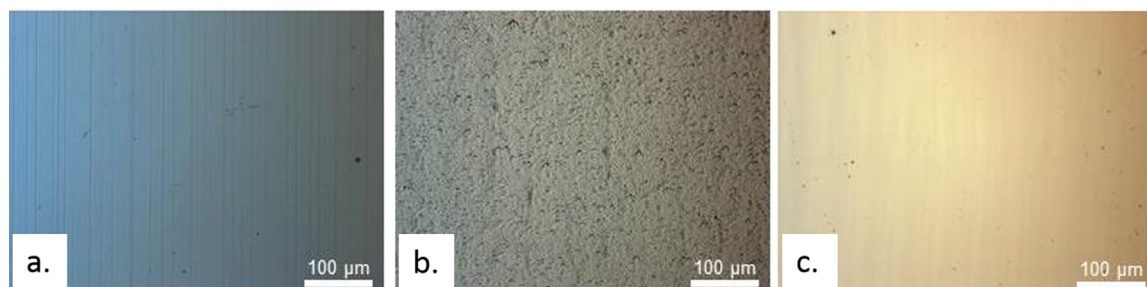


Fig. 11. The surface morphology of laser processed samples observed using optical microscopy representative of various power regimes: a) Below the melting threshold ($< 150 \text{ W}$), 20 \times ; b) A pockmarked surface in the 150–220 W range, 20 \times ; d) A deep-melted sample ($P > 220 \text{ W}$), 20 \times .

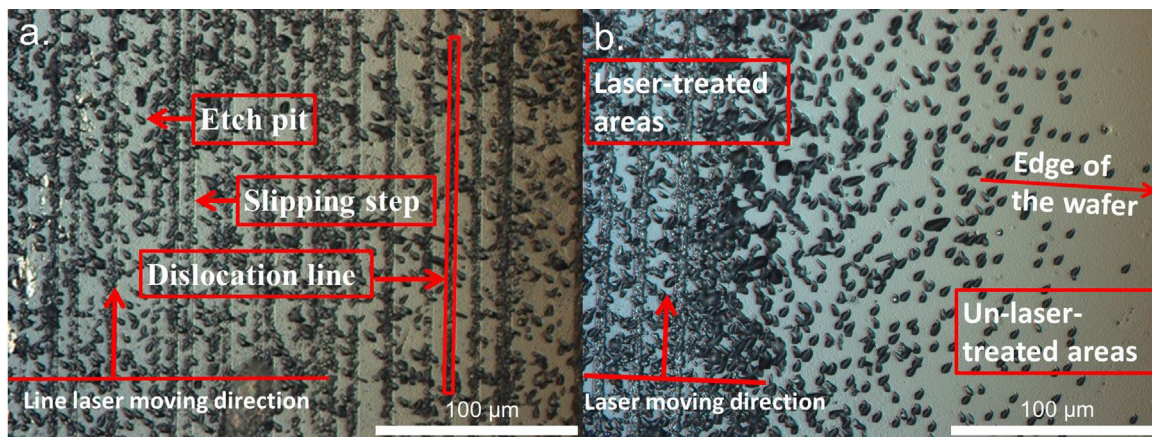


Fig. 12. a. A view at the middle of the laser scan of dense dislocation pits along slip steps for a low power (< 150 W) scanned sample after defect etching, $500\times$. b. Defect etching at the edge of the low power (< 150 W) laser scanned area.

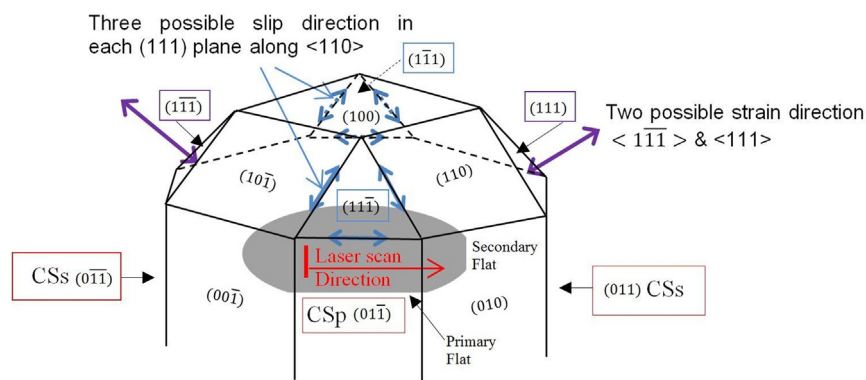


Fig. 13. The active slip system in (100) silicon wafer with respect to the laser scan direction and orientation of the silicon wafer sample. (For interpretation of the references to color in this figure, the reader is referred to the web version of this article.)

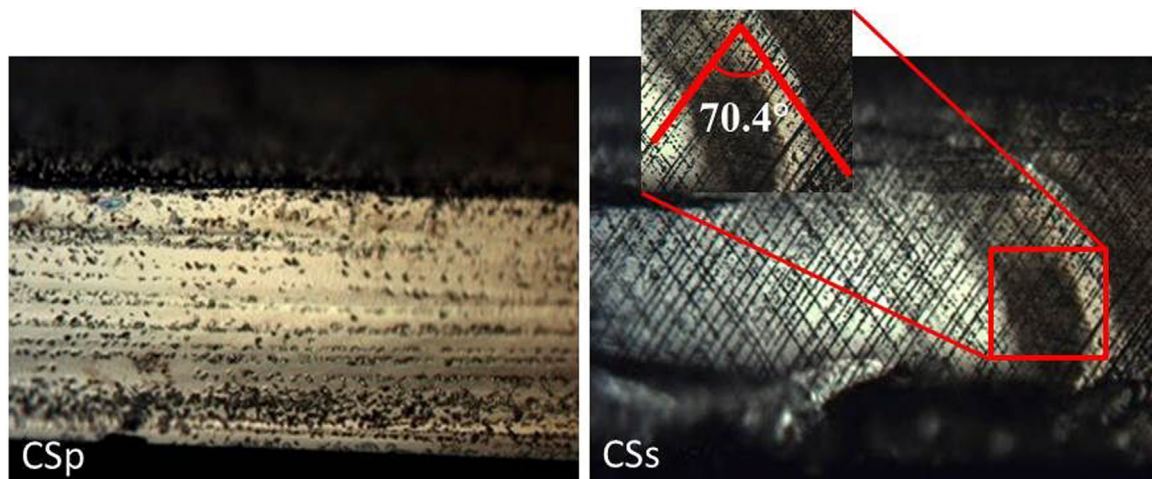


Fig. 14. The (110) cross-sectional view after Yang etching under an optical microscope of a bare silicon sample treated with low laser power, CSp (parallel to primary flat) on the left and CSs (parallel to secondary flat) on the right. The dislocation line angle measurement is shown in the inset.

junction depth experimentally achieved was measured by a cross-sectional etch technique and electrochemical capacitance-voltage measurement, which showed good agreement around $14\mu\text{m}$ for a sample treated with 246 W of total power. The junction depth of a laser treated sample measured by EBIC showed that the melt-based emitter formation resulted in a uniform thickness. An investigation of dislocation defects resulting from the laser process showed that these are plentiful and combine to create many slip steps along (111) planes. Most likely,

this is a result of the large temperature gradients that exist during laser processing. Realizing the benefits of a deep, low doped emitter created by laser melting will necessitate better control of these thermal gradients.

Acknowledgements

This work was supported by the Australian Renewable Energy

Agency through project RG123662-G "US-Australia Institute for Advanced Photovoltaics". The First author would like to thank the Australian Government Research Training Program for providing the PhD scholarship.

References

- [1] M.A. Green, *Solar Cells: Operating Principles: Technology, and System Applications*, Prentice-Hall, United States, 1982.
- [2] L. Mai, *Overcoming the Performance and Limitations of Commercial Screen-printed Solar Cells*, Ph.D. thesis, University of New South Wales (UNSW), Sydney, Australia, 2010.
- [3] A. Dastgheib-Shirazi, M. Steyer, G. Micard, H. Wagner, P.P. Altermatt, G. Hahn, Relationships between diffusion parameters and phosphorus precipitation during the POCl_3 diffusion process, *Energy Procedia* 38 (2013) 254–262.
- [4] H. Hannebauer, M. Sommerfeld, J. Müller, T. Dullweber, R. Brendel, Analysis of the emitter saturation current density of industrial type silver screen-printed front contacts, in: *Proceedings of the 27th EU PVSEC*, 2012, p. 1360.
- [5] A.W. Blakers, A. Wang, A.M. Milne, J. Zhao, M.A. Green, 22.8% efficient silicon solar cell, *Appl. Phys. Lett.* 55 (1989) 1363–1365.
- [6] J. Zhao, A. Wang, P. Altermatt, M.A. Green, Twenty-four percent efficient silicon solar cells with double layer antireflection coatings and reduced resistance loss, *Appl. Phys. Lett.* 66 (1995) 3636–3638.
- [7] E. Schneiderlochner, R. Preu, R. Luedemann, S.W. Glunz, Laser-fired rear contacts for crystalline silicon solar cells, *Prog. Photovolt. Res. Appl.* 10 (2002) 29–34.
- [8] M. Hermle, F. Feldmann, J. Eisenlohr, J. Benick, H. Steinkemper, A. Richter, B. Lee, P. Stradins, A. Rohatgi, S.W. Glunz, Approaching efficiencies above 25% with both sides-contacted silicon solar cells, in: *Proceedings of the 42nd Photovolt. Spec. Conf., IEEE*, 2015, pp. 1–3.
- [9] F. Feldmann, M. Bivour, C. Reichel, M. Hermle, S.W. Glunz, Passivated rear contacts for high-efficiency n-type Si solar cells providing high interface passivation quality and excellent transport characteristics, *Sol. Energy Mater. Sol. Cells* 120 (2014) 270–274.
- [10] M.A. Green, The passivated emitter and rear cell (PERC): from conception to mass production, *Sol. Energy Mater. Sol. Cells* 143 (2015) 190–197.
- [11] B. Min, H. Wagner, M. Müller, D.-H.N.P.P. Altermatt, Incremental efficiency improvements of mass-produced PERC cells up to 24%, predicted solely with continuous development of existing technologies and wafer materials, *EUPVSEC*, in: *Proc. 30th Eur. Photovolt. Sol. Energy Conf. Exhib.*, 2015.
- [12] M. Dahlinger, S.J. Eisele, P.C. Lill, J.R. Kohler, J.H. Werner, Full area laser doped boron emitter silicon solar cells, in: *Proceedings of the 38th Photovolt. Spec. Conf., IEEE*, 2012, pp. 1029–1031.
- [13] F. Cristiano, M. Shayesteh, R. Duffy, K. Huet, F. Mazzamuto, Y. Qiu, M. Quillec, H.H. Henrichsen, P.F. Nielsen, D.H. Petersen, Defect evolution and dopant activation in laser annealed Si and Ge, *Mater. Sci. Semicond. Process.* 42 (2016) 188–195.
- [14] S.F. Lombardo, S. Boninelli, F. Cristiano, G. Fisicaro, G. Fortunato, M.G. Grimaldi, G. Impellizzeri, M. Italia, A. Marino, R. Milazzo, Laser annealing in Si and Ge: anomalous physical aspects and modeling approaches, *Mater. Sci. Semicond. Process.* 62 (2017) 80–91.
- [15] B.J. Simonds, H.J. Meadows, S. Misra, C. Ferekides, P.J. Dale, M.A. Scarpulla, Laser processing for thin film chalcogenide photovoltaics: a review and prospectus, *J. Photonics Energy* 5 (2015).
- [16] Software is named for informational purposes only; it does not imply an endorsement or a recommendation by NIST.
- [17] COMSOL Multiphysics, Version 5.2a, 2017. Available from: <<http://www.comsol.com>>.
- [18] G. Fischer, K. Strauch, T. Weber, M. Müller, F. Wolny, R. Schiepe, A. Fülle, F. Lottspeich, S. Steckemetz, E. Schneiderlochner, Simulation based development of industrial PERC cell production beyond 20.5% efficiency, *Energy Procedia* 55 (2014) 425–430.
- [19] H. Hannebauer, T. Dullweber, U. Baumann, T. Falcon, R. Brendel, 21.2% efficient fineline printed PERC solar cell with 5 busbar front grid, *Phys. Status Solidi - Rapid Res. Lett.* 8 (2014) 675–679.
- [20] K.R. Catchpole, A.W. Blakers, Modelling the PERC structure for industrial quality silicon, *Sol. Energy Mater. Sol. Cells* 73 (2002) 189–202.
- [21] T.C. Röder, S.J. Eisele, P. Grabitz, C. Wagner, G. Kulshich, J.R. Köhler, J.H. Werner, Add-on laser tailored selective emitter solar cells, *Prog. Photovolt. Res. Appl.* 18 (2010) 505–510.
- [22] H. Antoniadis, F. Jiang, W. Shan, Y. Liu, All screen printed mass produced silicon ink selective emitter solar cells, in: *Proceedings of the 35th Photovolt. Spec. Conf. IEEE*, 2010, pp. 1193–1196.
- [23] COMSOL Multiphysics Reference Manual, 5.2a, Comsol Multiphysics, 2017.
- [24] J. Slotboom, H. de Graaff, Measurements of bandgap narrowing in Si bipolar transistors, *Solid. State Electron.* 19 (1976) 857–862.
- [25] W. Shockley, W.T. Read, Statistics of the recombinations of electrons and holes, *Phys. Rev.* 87 (1952) 835–842.
- [26] R.N. Hall, Electron-hole recombination in germanium, *Phys. Rev.* 87 (1952) 387.
- [27] P.A. Basore, D.T. Rover, A.W. Smith, PC-1D version 2: Enhanced numerical solar cell modelling, in: *Conf. Rec. Twent. IEEE Photovolt. Spec. Conf.*, 1988, pp. 389–396.
- [28] M.M. Hilali, A. Rohatgi, B. To, A review and understanding of screen-printed contacts and selective-emitter formation, in: *Proceedings of the 14th Work. Cryst. Silicon Sol. Cells Modul.*, 2004, pp. 80401–83393.
- [29] A. Cuevas, P.A. Basore, G. Giroult-Matlakowski, C. Dubois, Surface recombination velocity of highly doped n-type silicon, *J. Appl. Phys.* 80 (1996) 3370–3375.
- [30] P.P. Altermatt, J.O. Schumacher, A. Cuevas, M.J. Kerr, S.W. Glunz, R.R. King, G. Heiser, A. Schenk, Numerical modeling of highly doped Si: P emitters based on Fermi-Dirac statistics and self-consistent material parameters, *J. Appl. Phys.* 92 (2002) 3187–3197.
- [31] M.J. Kerr, J. Schmidt, C. Samundsett, A. Cuevas, Simplified PERC solar cells passivated with PECVD silicon nitride, in: *Proceedings of the 16th Eur. Photovolt. Sol. Energy Conference*, 2000.
- [32] J. Schmidt, M. Kerr, A. Cuevas, Surface passivation of silicon solar cells using plasma-enhanced chemical-vapour-deposited SiN films and thin thermal SiO_2 /plasma SiN stacks, *Semicond. Sci. Technol.* 16 (2001) 164.
- [33] C. Kranz, J.H. Petermann, T. Dullweber, R. Brendel, Simulation-based efficiency gain analysis of 21.2%-efficient screen-printed PERC solar cells, *Energy Procedia* 92 (2016) 109–115.
- [34] Z. Wang, P. Han, H. Lu, H. Qian, L. Chen, Q. Meng, N. Tang, F. Gao, Y. Jiang, J. Wu, Advanced PERC and PERL production cells with 20.3% record efficiency for standard commercial p-type silicon wafers, *Prog. Photovolt. Res. Appl.* 20 (2012) 260–268.
- [35] A. Metz, D. Adler, S. Bagus, H. Blanke, M. Bothar, E. Brouwer, S. Dauwe, K. Dressler, R. Droessler, T. Droste, Industrial high performance crystalline silicon solar cells and modules based on rear surface passivation technology, *Sol. Energy Mater. Sol. Cells* 120 (2014) 417–425.
- [36] H. Huang, J. Lv, Y. Bao, R. Xuan, S. Sun, S. Sneek, S. Li, C. Modanese, H. Savin, A. Wang, 20.8% industrial PERC solar cell: ALD Al_2O_3 rear surface passivation, efficiency loss mechanisms analysis and roadmap to 24%, *Sol. Energy Mater. Sol. Cells* 161 (2017) 14–30.
- [37] C.H. Wang, K. Misiakos, A. Neugroschel, Minority-carrier transport parameters in n-type silicon, *IEEE Trans. Electron Devices* 37 (1990) 1314–1322.
- [38] K.R. McIntosh, S.C. Baker-Finch, OPAL 2: Rapid optical simulation of silicon solar cells, in: *Proceedings of the 38th Photovolt. Spec. Conf., IEEE*, 2013, pp. 265–271.
- [39] T. Dullweber, H. Hannebauer, S. Dorn, S. Schimanke, A. Merkle, C. Hampe, R. Brendel, Emitter saturation current densities of 22 A/cm^2 applied to industrial PERC solar cells approaching 22% conversion efficiency, *Prog. Photovolt. Res. Appl.* (2016).
- [40] P. Saint-Cast, S. Werner, J. Greulich, U. Jäger, E. Lohmüller, H. Höfler, R. Preu, Analysis of the losses of industrial-type PERC solar cells, *Phys. Status Solidi* 214 (2017).
- [41] L.-C. Cheng, M.-C. Kao, H.-H. Huang, P.-S. Huang, L.-W. Cheng, 21% p-type industrial PERC cells with homogeneous emitter profile and thermally grown oxidation layer, in: *Proceedings of the 42nd Photovolt. Spec. Conf., IEEE*, 2015, pp. 1–3.
- [42] R.B. Fair, J. Tsai, A quantitative model for the diffusion of phosphorus in silicon and the emitter dip effect, *J. Electrochem. Soc.* 124 (1977) 1107–1118.
- [43] H. Koda, Diffusion coefficients of impurities in silicon melt, *Jpn. J. Appl. Phys.* 2 (1963) 212.
- [44] B.J. Simonds, A. Teal, T. Zhang, J. Hadler, Z. Zhou, S. Varlamov, I. Perez-Würfl, Dual-beam laser thermal processing of silicon photovoltaic materials, *Proc. SPIE - Int. Soc. Opt. Eng.* (2016) 973505–973508.
- [45] T. Satō, Spectral emissivity of silicon, *Jpn. J. Appl. Phys.* 6 (1967) 339.
- [46] M.A. Green, M.J. Keever, Optical properties of intrinsic silicon at 300 K, *Prog. Photovolt.* 3 (1995) 189–192.
- [47] M.O. Lampert, J.M. Koebel, P. Siffert, Temperature dependence of the reflectance of solid and liquid silicon, *J. Appl. Phys.* 52 (1981) 4975–4976.
- [48] P.D. Desai, Thermodynamic properties of iron and silicon, *J. Phys. Chem. Ref. Data* 15 (1986) 967.
- [49] Z. Zhou, S. Mukherjee, W.K. Rhim, Measurement of thermophysical properties of molten silicon using an upgraded electrostatic levitator, *J. Cryst. Growth* 257 (2003) 350–358.
- [50] H. Sasaki, E. Tokizaki, K. Terashima, S. Kimura, Density measurement of molten silicon by an improved Archimedian method, *J. Cryst. Growth* 139 (1994) 225–230.
- [51] H. Sasaki, E. Tokizaki, K. Terashima, S. Kimura, Density variation of molten silicon measured by an improved archimedian method, *Jpn. J. Appl. Phys.* 33 (1994) 3803–3807.
- [52] S. Kawanishi, H. Sasaki, K. Terashima, S. Kimura, Effect of impurity doping on density anomalies in molten silicon, *Japanese, J. Appl. Phys. Part 2 Lett.* 34 (1995) L1509–L1512.
- [53] K. Ohsaka, S. Chung, Densities of Si determined by an image digitizing technique in combination with an electrostatic levitator, *Appl. Phys. Lett.* 70 (1997) 423–425.
- [54] K. Mukai, Z. Yuan, Measurement of the density of molten silicon by a modified sessile drop method, *JIM, Mater. Trans.* 41 (2000) 323–330.
- [55] Y. Sato, T. Nishizuka, K. Hara, T. Yamamura, Y. Waseda, Density measurement of molten silicon by a pycnometric method, *Int. J. Thermophys.* 21 (2000) 1463–1471.
- [56] W. Xu, H.C. Sun, J. Xu, W. Li, W.W. Mu, Y. Liu, M.Y. Yan, X.F. Huang, K.J. Chen, Electroluminescence with micro-watt output from ultra-small sized Si quantum dots/amorphous SiO_2 multilayers prepared by laser crystallization method, *Appl. Surf. Sci.* 258 (2011) 346–349.
- [57] M. Watanabe, M. Adachi, T. Morishita, K. Higuchi, H. Kobatake, H. Fukuyama, Does supercooled liquid Si have a density maximum? *Faraday Discuss.* 136 (2007) 286–328 (279).
- [58] N.A. Vatolin, O.A. Yesin, Density of molten alloys of manganese with silicon, iron and carbon, *Phys. Met. Metallogr.* 16 (1963) 129–130.
- [59] Y.B. Magomedov, G.G. Gadjiev, High-temperature thermal conductivity of silicon in the solid and liquid states, *High Temp.* 46 (2008) 422–424.
- [60] C.J. Glassbrenner, G.A. Slack, Thermal Conductivity of Si and Ge from 3 K to the melting point, *Phys. Rev.* 134 (1964) A1058–A1069.
- [61] D.S. Beers, G.D. Cody, B. Abeles, Thermal conductivity of Ge, Si and III-V

- compounds at high temperatures, *Proc. Intern. Conf. Phys. Semicond.* (1962) 41–48.
- [62] M.L.V. Gayler, Melting point of high-purity silicon, *Nature* 142 (1938) 478.
- [63] F. Hoffman, A. Schulze, No Title, *Phys. Z.* 38 (1938) 901–905.
- [64] P.B. Kantor, O.M. Kisel, E.M. Fomichev, No Title, *Ukr. J. Phys.* 5 (1960) 358–362.
- [65] *Metal Handbook - Properties and Selection: Iron and Steel*, 9th ed., American Society for Metals, Oshio, 1978.
- [66] J.G. Hurst, R.L. Powell, D.H. Weitzel, Thermal conductivity standard reference materials from 4 to 300 K. I. Armco iron: including apparatus description and error analysis, *J. Res. Natl. Bur. Stand. - A. Phys. Chem.* 74A (1970) 673–690.
- [67] D.C. Wallace, P.H. Sidles, G.C. Danielson, Specific heat of high purity iron by a pulse heating method, *J. Appl. Phys.* 31 (1960) 168–176.
- [68] K.H. Yang, An etch for delineation of defects in silicon, *J. Electrochem. Soc.* 131 (1984) 1140–1145.
- [69] M.W. Jenkins, A new preferential etch for defects in silicon crystals, *J. Electrochem. Soc.* 124 (1977) 757–762.
- [70] M. Fathi, Delineation of crystalline extended defects on multicrystalline silicon wafers, *Int. J. Photoenergy* (2007).
- [71] M.W. Jenkins, A new preferential etch for defects in silicon crystals, *J. Electrochem. Soc.* 124 (1977) 757–762.
- [72] H.J. Leamy, Charge collection scanning electron microscopy, *J. Appl. Phys.* 53 (1982) R51–R80.
- [73] E. Peiner, A. Schlachetzki, D. Krüger, Doping profile analysis in Si by electrochemical capacitance-voltage measurements, *J. Electrochem. Soc.* 142 (1995) 576–580.
- [74] F.M. Smits, Measurement of sheet resistivities with the four-point probe, *Bell Labs Tech. J.* 37 (1958) 711–718.
- [75] I. Yonenaga, An overview of plasticity of Si crystals governed by dislocation motion, *Eng. Fract. Mech.* 147 (2015) 468–479.
- [76] K. Sumino, Deformation behavior of silicon, *Metall. Mater. Trans. A Phys. Metall. Mater. Sci.* 30 (1999) 1465–1479.
- [77] S.M. Hu, Dislocations in thermally stressed silicon wafers, *Appl. Phys. Lett.* 22 (1973) 261–264.
- [78] M.F. Ashby, D.R.H. Jones, *Engineering Materials 1: An Introduction to their Properties and Applications*, 2nd ed., Butterworth Heinemann, Woburn, 1996.
- [79] E. Billig, Some defects in crystals grown from the melt. I. defects caused by thermal stresses, *Proc. R. Soc. London A Math. Phys. Eng. Sci. R. Soci.* (1956) 37–55.
- [80] D. Chen, *Improved Performance of Low-Cost Silicon Substrates through Advanced Laser Processing*, Thesis, University of New South Wales, Sydney, Australia, 2016.
- [81] M. Abbott, P. Cousins, F. Chen, J. Cotter, Laser-induced defects in crystalline silicon solar cells, in: *Proceedings of Conf. Rec. Thirty-First IEEE Photovolt. Spec. Conf., IEEE*, 2005, pp. 1241–1244.